PAPER

A multiple cancer cell optical biosensing metastructure realized by CPA

Jia-Hao Zou, Jun-Yang Sui, [ID] You-Ran Wu [ID] and Hai-Feng Zhang [ID] *

A one-dimensional optical biosensing metastructure (OBM) with graphene layers is presented in this paper. It is realized by coherent perfect absorption (CPA) and operates in the transverse electric mode. It shows a strong linear fitting relationship between the refractive index (RI) of the analysis layer and the frequency corresponding to the absorption peak, and the R-square is up to 1. Additionally, based on the principle of CPA, the OBM can realize the function of multiple cancer cell detection by adjusting the detection range by controlling the phase difference of coherent electromagnetic waves. Its detection ranges are 1.34–1.355 and 1.658–1.662. Thanks to its high-quality factor, great figure of merit, and low detection limit, whose best values are, respectively, 6.9×10^4, 1.2×10^4 RIU^{-1}, and 3.6×10^{-6} RIU, the detection of weak changes in the RI of a cancer cell is possible. Additionally, its sensitivity can reach 26.57 THz RIU^{-1}. This OBM based on CPA has major implications for advancing the study and investigation into the application of CPA. It also provides a simple and efficient approach to distinguish cancer cells and may be widely used in the biomedical field.

1. Introduction

Coherent perfect absorption (CPA) is a captivating research area within the field of optics because of its significant applications in light control and modulation.[1–3] The concept of CPA relies on the principles of interference in optics. When a beam of electromagnetic waves (EWs) illuminates the surface of an object, a portion of the EWs are reflected, while the rest is absorbed. In conventional scenarios, the ratio between absorption and reflection remains fixed. However, by precisely controlling the phase difference and amplitude ratio between the incident and reflected EWs, CPA can be achieved. By designing specific structures based on CPA, researchers can attain highly selective absorption and modulation of EWs. This technology holds immense potential in areas such as fiber-optic metadevices,[4] logic units,[5] and sensors.[6] Based on CPA, a biosensor with a large measuring range is small in size and can detect in real-time.[7] This will improve technical approaches to effectively preventing disease. Furthermore, CPA is not a proxy for, but a complement to, traditional modulation methods. The coexistence of CPA and traditional modulation methods, like the applied voltage on graphene,[5] is allowed.

Cancer, a formidable and complex group of diseases, remains one of the most significant challenges to human health in the modern world.[8] Unlike healthy cells, cancer cells

divide uncontrollably, forming malignant tumors that can infiltrate nearby tissues and organs or travel through the bloodstream and lymphatic system to establish secondary growth, known as metastasis, in distant parts of the body.[9] Because cancer may spread throughout the body and ultimately kill the patient,[10] early detection of abnormal cells is crucial. The enzyme-linked immunosorbent assay has been employed as the gold standard method for cancer diagnosis for more than 40 years.[11] However, because this method relies on labels, it is problematic for simple "point of care" (POC) detection. Furthermore, it is typically accompanied by protracted waiting times and challenging microscopic examinations. The quick treatment and recovery of patients may be seriously hampered by these limitations in particular situations (such as emergency medicine or critical care), but labeling takes up a lot of time and resources. For the rapid, label-free, portable, and multiplexed detection of tumor biomarkers and cancer cells, it is essential to develop ultrasensitive and selective biosensors. Due to the light interaction between the light field and the organelles, the cell RI can be used to quantify the chemical composition within the cell structure.[12,30] The rapid division and proliferative activity of cancer cells leads to a high concentration of protein molecules in the organelles, leading to an increase in the cell RI.[12,30] So, this difference of RIs between normal and cancer cells is thought to be a useful criterion for the quantitative detection of cell malignancy. Moreover, because different kinds of cells contain different amounts of proteins,[12] they have different RIs. Therefore, this is thought to be a useful criterion for the detection of cell types, including

College of and Optical Engineering & College of Flexible Electronics (Future Technology), Nanjing University of Posts and Telecommunications, Nanjing, 210023, China. E-mail: hanlor@163.comor, hanlor@njupt.edu.cn

cancer cells. Choi *et al.* presented the feasibility of identifying cancer cells by measuring the refractive index (RI) distribution across a single live cell with ultrahigh resolution full-field optical coherence microscopy (FF-OCM).[30]

Because of the advantages of being compact and portable, the optical biosensing metastructure (OBM) has been widely studied in recent years.[13] Romano *et al.*[14] designed an OBM for protein sensing based on photonic crystals supporting bound states in the continuum. Ghorbani *et al.*[15] developed a novel OBM based on numerical techniques for monitoring glucose content in various samples. Sui *et al.*[16] put forward new ideas for the photonic spin Hall effect and designed an OBM with multiple functions based on it. These works are extremely important for the advancement of biosensing, and they provide a unique idea for the research of OBMs. But these studies only realize a single sensing range and the sensing range cannot be changed by phase control. There is a lack of research on OBMs for multiple cancer cells, especially the OBM with a high quality-factor (Q). Moreover, the OBM with CPA is rarely discussed in publications. This will restrict the potential areas for associated field studies.

A one-dimensional (1-D) OBM with CPA is presented in this paper. To obtain absorption peaks (APs) with high Q, graphene layers (GLs) are added to the OBM as the defect layers. The frequency (f) comparable to the AP will move when the refractive index (RI) of the analysis layer varies. It possesses a strong linear fitting relationship (LFR) and excellent performance, whose R-square and Q can, respectively, reach 1 and 6.9×10^4, respectively. So, the detection of weak changes in the RI is possible, thanks to the LFR between the RI and f. Furthermore, the OBM can achieve measurements for different RI ranges containing RIs of various cell groups by adjusting the phase difference of coherent EWs. So, it can realize the function of multiple cancer cell detection. This work provides a new way for the application of CPA. It also offers a simple and efficient approach to distinguishing cancer cells in medicine. Additionally, it should be noted that experimental verification cannot be done due to financial constraints and unfavorable experimental circumstances. So, this paper focuses on theoretical innovation and demonstrates the point of view of simulation-based results. All of the conclusions in this paper are based on previously acknowledged research and were computed using software that is widely accepted in the field. Thus, the findings in this paper are reliable.

2. Structure design and calculation formula

2.1 The structure of the OBM

To display the structure of the proposed OBM clearly, different mediums are colored in a variety of hues in Fig. 1. The OBM is made up of ordinary dielectrics A, B, and C, two combination layers (CLs), and an analysis layer. Among them, dielectric A is barium strontium titanate (BST) doped with 10 *wt*% magnesium oxide (MgO), and the value of the RI is $n_A = 16.49$.[17] Titanium dioxide (TiO$_2$) and lithium chloride (LiCl) are the respective components of dielectrics B and C, and their respective RI values are 2.76[18] and 1.69.[19] Every CL is staggered by GLs and silicon dioxide (SiO$_2$) layers like SiO$_2$ (GLSiO$_2$).[3]
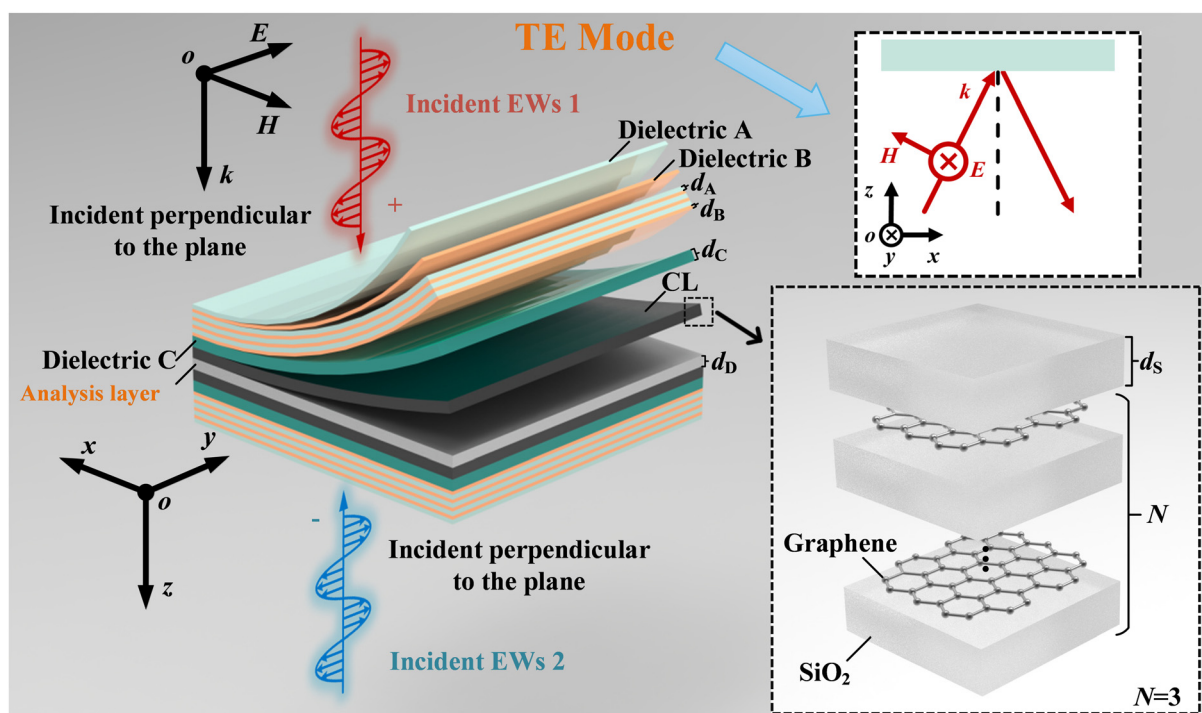

Fig. 1 Schematic diagram of the 1-D OBM which is made up of different dielectric layers (two TE EWs incident perpendicular to the plane).

4448 | *Phys. Chem. Chem. Phys.*, 2024, 26, 4447–4454

This journal is © the Owner Societies 2024

Table 1 The detailed geometrical dimensions of the OBM

Parameters	d_A	d_B	d_C	d_D	d_S
Value (μm)	0.4	0.3	1	3	0.01

The CL is a periodic structure, and the value of the period number N is 3. The RI of SiO_2 is n_S, and its value is 1.5.[20] The thickness of the GL is only the size of a carbon atom molecule (diameter: 0.34 nm[21]). Moreover, the chemical potential μ_C of the GL can significantly affect the RI of the GL and the value of μ_C is 0.001 eV in this paper due to no voltage applied to the OBM.[22] The two CLs are located on both sides of the analysis layer (see Fig. 1). d_i (i indicates A, B, C, D, or S) expresses the thickness of the dielectric layers. The detailed geometrical dimensions of the structure are shown in Table 1. When the OBM is working, the EWs are incident perpendicular to the xoy-plane in Fig. 1.

The layered structure proposed in this work is a theoretical design that seeks theoretical effects and favors theoretical effects above manufacturing. But, if specific manufacturing is required, it can be done as in ref. 23. As can be seen from Fig. 2, the layered structure of the OBM can be realized using etching.

A silicon wafer is chosen as the substrate, and using the wet anisotropic etching process, vertical grooves of varying widths are then etched into the silicon wafer in line with the scales of the two materials.[23] More specifically, during the etching process, which can be carried out using a 44 wt% potassium hydroxide (KOH) aqueous solution at 85 °C, the thermally produced SiO_2 layer can act as the hard mask.[23] Once the silicon substrate has produced grooves that comply with the predefined parameters of theoretical research, the right material can be placed at the proper location. Theoretically, a substrate is said to have the best form when it can expand in both height and width without being constrained and when the properties of this structure match those predicted by the theoretical analysis.[23]

2.2 The calculation formula of graphene

Intraband σ_{intra} and interband σ_{inter} interactions determine the conductivity σ of graphene:[24]

$$\sigma_{intra} = \frac{ie^2 k_B T}{\pi \hbar^2 (\omega + i/\tau)}\left(\frac{\mu_C}{k_B T} + 2\ln\left(e^{-\frac{\mu_C}{k_B T}} + 1\right)\right), \quad (1)$$
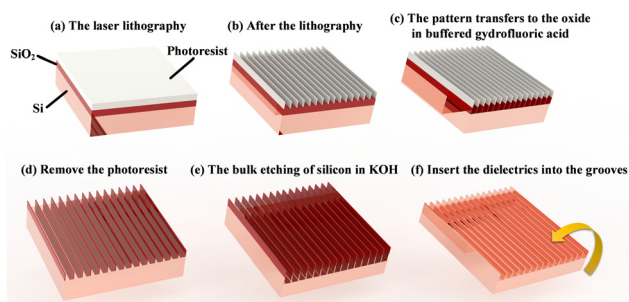

Fig. 2 The flow diagrams of the fabrication process of the proposed layered structure.

$$\sigma_{inter} = \frac{ie^2}{4\pi\hbar}\ln\left(\frac{2|\mu_C| - \hbar(\omega + i/\tau)}{2|\mu_C| + \hbar(\omega + i/\tau)}\right), \quad (2)$$

$$\sigma = \sigma_{intra} + \sigma_{inter}, \quad (3)$$

$$\sigma = \frac{ie^2 k_B T}{\pi \hbar^2 (\omega + i/\tau)}\left(\frac{\mu_C}{k_B T} + 2\ln\left(e^{-\frac{\mu_C}{k_B T}} + 1\right)\right)$$
$$+ \frac{ie^2}{4\pi\hbar}\ln\left(\frac{2|\mu_C| - \hbar(\omega + i/\tau)}{2|\mu_C| + \hbar(\omega + i/\tau)}\right), \quad (4)$$

where ω, k_B, e, and $\hbar$ correspond to the angular f, Boltzmann constant, electron charge, and reduced Planck constant, respectively.[24] Imaginary unit i is $(-1)^{1/2}$, and relaxation time τ is 1×10^{-13} s.[24] Moreover, the entire construction is exposed to air at a temperature of 293 K to study the general environment. So, the value of temperature T is 293 K. The effective dielectric constant ε_g can be written as[24]

$$\varepsilon_g = 1 + \frac{i\sigma}{\omega\varepsilon_0 d_g}, \quad (5)$$

where ε_0 is the vacuum permittivity constant and the thickness of graphene is $d_g = 0.34$ nm.[21] In addition, the RI of graphene can be indicated as $n_g = (\varepsilon_g)^{1/2}$.

2.3 The calculation formula of CPA

Graphene mostly responds to the transverse electric field component of the reaction, but the longitudinal magnetic field component of the reaction is less significant.[25] Therefore, the focus of this work is on investigating performance in the transverse electric (TE) mode. In this mode, the wave vector k and the y-axis form a plane where the electric field of the EWs in Fig. 1 vibrates along the y-axis and the magnetic field vector is perpendicular to the plane. To reduce the computational complexity and improve the computational efficiency, while still getting the main response features of graphene, the performance of EWs under the TE mode is only explored in this paper. The matrix belonging to the propagation of EWs in the ordinary dielectric layer and graphene layer can be expressed as[26]

$$\mathbf{M}_j = \begin{pmatrix} \cos(k_{jz}d_j) & -\frac{i}{\eta_j}\sin(k_{jz}d_j) \\ -i\eta_j \sin(k_{jz}d_j) & \cos(k_{jz}d_j) \end{pmatrix}, \quad (6)$$

where $k_{jz} = \omega/c n_j \cos\theta_j$ is the component of the wave vector in the z-axis and c is the speed of light in a vacuum. In eqn (6), d_j and n_j, respectively, represent the thickness and the RI of every dielectric layer, and j indicates A, B, C, D, S, or g. For TE polarization, the optical admittance is η_i, and $\eta_i = (\varepsilon_0/\mu_0)^{1/2} n_i \cos\theta_i$, where μ_0 is the permeability in a vacuum. Therefore, the entire transfer matrix $\mathbf{M}$ can be given as

$$\mathbf{M} = (\mathbf{M}_A\mathbf{M}_B)^4 \mathbf{M}_C\mathbf{M}_S(\mathbf{M}_g\mathbf{M}_S)^3\mathbf{M}_D\mathbf{M}_S(\mathbf{M}_g\mathbf{M}_S)^3\mathbf{M}_C(\mathbf{M}_B\mathbf{M}_A)^4 \quad (7)$$

the results can be written as follows:

$$\mathbf{M} = \begin{pmatrix} M_{11} & M_{12} \\ M_{21} & M_{22} \end{pmatrix}, \quad (8)$$

This journal is © the Owner Societies 2024

Phys. Chem. Chem. Phys., 2024, **26**, 4447–4454 | **4449**

and the transmissivity coefficient (t) and the reflection coefficient (r) can be calculated using the following equations:[26]

$$r = \frac{\eta_0(M_{11} + \eta_0 M_{12})) - (M_{21} + \eta_0 M_{22})}{\eta_0(M_{11} + \eta_0 M_{12}) + (M_{21} + \eta_0 M_{22})}, \quad (9)$$

$$t = \frac{2\eta_0}{\eta_0(M_{11} + \eta_0 M_{12}) + (M_{21} + \eta_0 M_{22})}, \quad (10)$$

due to exposure to air, the positive and negative backgrounds are the same. So there is $\eta_0 = \eta_{N+1} = (\varepsilon_0/\mu_0)^{1/2} n_0/\cos\theta_0$.

As can be seen from Fig. 1, the given OBM is symmetrical. Thus, the t and r of positive and negative scales are equivalent in terms of their numerical values, and they can be shown as $r_+ = r_- = r$ and $t_+ = t_- = t$. In this paper, EW 1 propagating along the positive direction of the z-axis is defined as the positive scale (+). In contrast, EW 2 propagating along the negative direction of the z-axis is defined as the negative scale (−). Both the transmitted EWs from the incident EWs on the other side and the reflected EWs from the incident EWs on this side make up the observed EWs on each side. The following scattering matrix **S** can be used to explain this relationship:[27]

$$\begin{pmatrix} O_+ \\ O_- \end{pmatrix} = \mathbf{S}\begin{pmatrix} I_+ \\ I_- \end{pmatrix} = \begin{pmatrix} t & r \\ r & t \end{pmatrix}\begin{pmatrix} I_+ \\ I_- \end{pmatrix}, \quad (11)$$

where I_+ and I_- are the intensities of two incident electromagnetic waves and eqn (11) can also be written as[27]

$$O_+ = t|I_+|e^{i\varphi_+} + r|I_-|e^{i\varphi_-}, \quad (12)$$

$$O_- = r|I_+|e^{i\varphi_+} + t|I_-|e^{i\varphi_-}, \quad (13)$$

where φ_+ and $\varphi-$ are the phases of two incident waves. So, the absorption (A) can be written as[27]

$$A = 1 - \frac{|O_+|^2 + |O_-|^2}{|I_+|^2 + |I_-|^2}. \quad (14)$$

The intensities of two coherent beams of EWs are the same in this paper, and the calculation formula of CPA can be expressed as follows according to eqn (12)–(14):

$$A = 1 - (|t| - |r|^2) - |t||r|(1 + \cos\Delta\varphi_1 \cos\Delta\varphi_2) \quad (15)$$

where $\Delta\varphi_1 = \text{Arg}(t) - \text{Arg}(r)$, and $\Delta\varphi_2 = \varphi_+ - \varphi_-$. "Arg()" is used to represent the argument principal value of the plural.

3. Design and simulation results

3.1 Production of sharp APs

Q is a crucial parameter used to assess the efficiency and selectivity of resonant systems and filters:[28]

$$Q = \frac{f_T}{\text{FWHM}}, \quad (18)$$

where f_T implies the f of the absorption peak (AP) and FWHM symbolizes the half-height width of the resonant peak.[28] A higher Q indicates a better performance of the OBM.
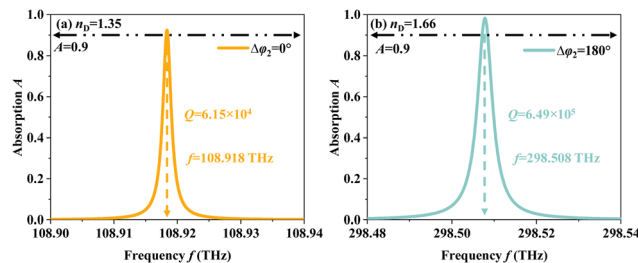

Fig. 3 The diagrams of sharp APs forming based on CPA (dashed dotted line is the contour of $A = 0.9$). (a) In the case of $\Delta\varphi_2 = 0°$ and $n_D = 1.35$. (b) In the case of $\Delta\varphi_2 = 180°$ and $n_D = 1.66$.

Based on eqn (15), the APs forming based on the CPA of the OBM at different fs are calculated. When the value of $\Delta\varphi_2$ is 0°, a sharp AP forms at about $f = 108.92$ THz in the case of $n_D = 1.66$. As can be seen from Fig. 3(a), its Q is 6.15×10^4, and the value of A is larger than 0.9. The condition of the sharp AP, which is produced at about $f = 298.51$ THz in the case of $\Delta\varphi_2 = 180°$ and $n_D = 1.66$, is displayed in Fig. 3(b). Its Q reaches up to 6.49×10^4 and A is close to 1. The high values of Q prove that the selectivity of the OBM is excellent.

The period number N of the CLs plays an important role in the result. The effect of N on the APs is shown in Fig. 4. As can be seen in Fig. 4(a), the value of A in the case of $\Delta\varphi_2 = 0°$ and $n_D = 1.35$ drops down as the number of N increasing in the range of 3–5. When $N = 4$, the A of the AP decreases to about 0.7, smaller than 0.9. In the case of $N = 5$, A drops further to about 0.45. So, this will cause the OBM, mentioned above, to lose efficacy and fail. Compared to the N values of 1 and 2, shown in Fig. 4(b), when the value of N is 3 in the case of $\Delta\varphi_2 = 180°$ and $n_D = 1.66$, the A value of the AP is larger. When the value of N is set to 2, A decreases to 0.9. The A value of the AP drops further to 0 in the case of $N = 1$. This demonstrates that the performance of the OBM is better when N is set to 3.

For the indicators of graphene, its μ_C is very important. Fig. 5 demonstrates the difference in the APs under the different cases of μ_C when the values of μ_C are 0.001 eV, 0.2 eV, and 0.4 eV. As can be seen from Fig. 5(a), in the case of $\Delta\varphi_2 = 0°$, the values of A are approximately equal when the values of μ_c are 0.001 eV and 0.2 eV. But, when the value of μ_C is up to 0.4 eV, the value of A drops rapidly to 0.15. Fig. 5(b) shows
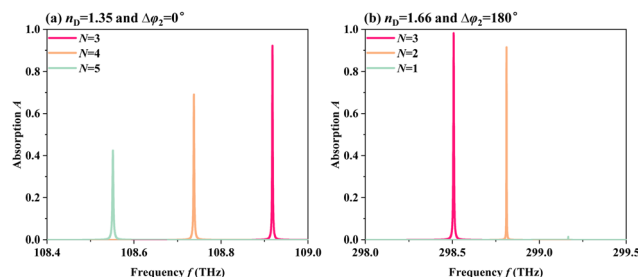

Fig. 4 The effects of different N values on the APs. (a) The APs when the values of N are 3, 4, and 5 in the case of $\Delta\varphi_2 = 0°$ and $n_D = 1.35$. (b) The APs when the values of N are 1, 2, and 3 in the case of $\Delta\varphi_2 = 180°$ and $n_D = 1.66$.

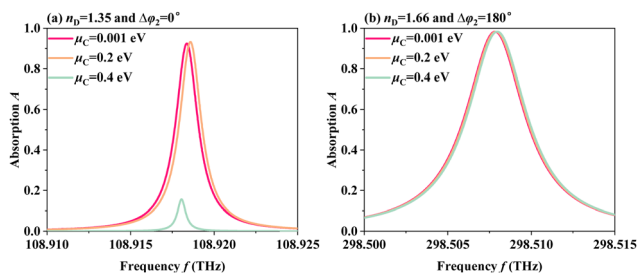4450 | *Phys. Chem. Chem. Phys.*, 2024, **26**, 4447–4454

This journal is © the Owner Societies 2024

Fig. 5 When the values of μ_C are 0.001 eV, 0.2 eV, and 0.4 eV, the effect belonging to different μ_C values of GLs on the APs. (a) The APs in the case of $\Delta\varphi_2 = 0°$ and $n_D = 1.35$. (b) The APs in the case of $\Delta\varphi_2 = 180°$ and $n_D = 1.66$.

the effect of μ_C on the APs in the case of $\Delta\varphi_2 = 180°$. As μ_C increases in the range of 0.001–0.4 eV, the values of A are approximately equal, which are near 1. But controlling μ_C requires applying a voltage to the OBM,[22] which increases the difficulty of manufacturing. So, the μ_C of graphene in this paper is set to 0.001 eV to improve the performance of the OBM.

Fig. 6 displays that the A value of the AP can be enhanced by precisely controlling the $\Delta\varphi_2$ between coherent EWs. The f value of the AP is about 108.92 THz when n_D is defined as 1.35. As can be seen from Fig. 6(a), the maximum AP, which can enhance the quality of the OBM, is generated when the value of $\Delta\varphi_2$ is 0°, and the value of A is 0.92. However, the maximum value of the AP continually declines as $\Delta\varphi_2$ improves. When the value of $\Delta\varphi_2$ is 120°, the value of the AP drops down to 0.23. Fig. 6(b) exhibits the maximum AP generated when the value of $\Delta\varphi_2$ is 180° in the case of $n_D = 1.66$. As $\Delta\varphi_2$ drops, the value of the AP decreases, which may degrade the performance of cancer detection. If $\Delta\varphi_2$ is set to 90°, the value will drop to 0.49, which is far below the threshold ($A = 0.9$). Because of these, the two modes of the OBM for cancer cell detection are under the condition of $\Delta\varphi_2 = 0°$ and $\Delta\varphi_2 = 180°$.

To more clearly analyze the propagation of EWs in the OBM and explain the reasons for sharp AP formation, two electric field intensity distribution maps in the case of $\Delta\varphi_2 = 0°$ and n_D
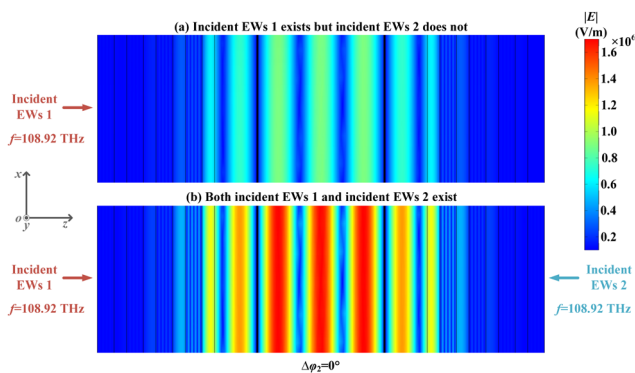

Fig. 7 The electric field intensity distribution maps when the f of EWs is 108.92 THz. (a) Incident EW 1 exists but incident EW 2 does not. (b) Both incident EW 1 and incident EW 2 exist, and $\Delta\varphi_2$ is 0°.

= 1.35 are plotted and shown in Fig. 7. As can be seen from Fig. 7, the intermediate layer (the analysis layer in Fig. 1), which is added to the OBM as a defect layer, creates a microcavity and a small passband in the photonic band gap.[28] The presence of the CL on its both sides further concentrates the energy of EWs in the middle of the structure. Additionally, the electric field intensity when two incident coherent EWs are relative, as can be observed from Fig. 7(b), is larger than that in the case of only one beam of incident EWs, whose electric field intensity distribution is illustrated in Fig. 7(a). According to the principle of CPA, when two coherent EWs are incident in different directions, there is a higher local field augmentation effect, which results in a strong absorption characteristic at the defect position.[28] Thus, sharp APs like those in Fig. 3 are produced.

3.2 Multiple cancer cell detection

The values of n_D are different when different kinds of cells are put in the analysis layer. So, the OBM is able to distinguish normal and cancer cells based on the RI. Table 2 displays the five groups of cell types to be measured in this paper.[29,30] Tables 3 and 4 show the RIs corresponding to different cell

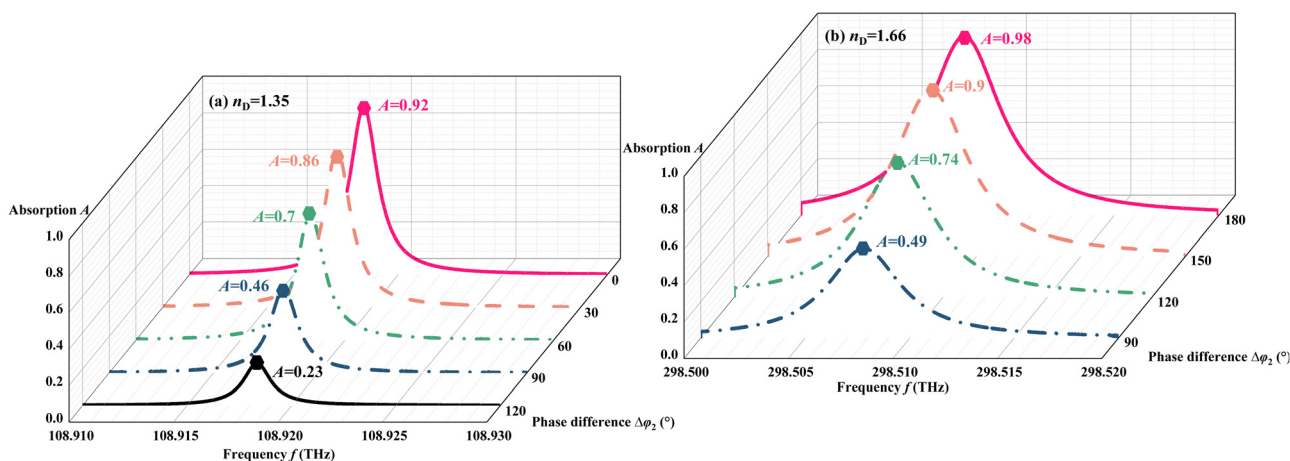

Fig. 6 The effects of different phases $\Delta\varphi_2$ on the Aps: (a) in the case of $n_D = 1.35$ and (b) in the case of $n_D = 1.66$.

This journal is © the Owner Societies 2024

Phys. Chem. Chem. Phys., 2024, **26**, 4447–4454 | **4451**

Table 2 Five groups of cell types to be measured in this paper[29,30]

Group	Normal	Cancer
Rat kidney cells	RK3E	RK3E-ras
Human oral squamous cells	INOK	YD-10B
Human gastric cells	GES-1	MGC-803
Human liver cells	LO2	7721
Human epidermal cells	HEM	MEL

Table 4 The RI of detection cell types when $\Delta\varphi_2$ is controlled to 180°[30]

Type	RI (RIU)	Error (RIU)
GES-1	1.66020	2.9×10^{-5}
MGC-803	1.66149	2.8×10^{-5}
LO2	1.66040	2.6×10^{-5}
7721	1.66109	2.6×10^{-5}
HEM	1.66067	2.8×10^{-5}
MEL	1.66179	2.9×10^{-5}

types which can be distinguished, respectively, on the different modes by the given OBM.

Frequency modulation is the most often used technique due to its usefulness in observation and experimentation. A difficult-to-detect biological signal can be converted into an observable photoelectric signal by establishing a specific linear relationship between f and the variable to be monitored. If the signal of biology changes, a precise movement in the f of the AP will result. The location of the associated AP can be used to derive specific information about biology, which is also how the OBM functions. Crucial metrics to take into account when assessing an OBM include sensitivity (S), Q, the figure of merit (FOM), and the detection limit (DL). A good OBM has a greater S, higher Q, greater FOM, and lower DL. Associated definitions can be stated as follows:[28]

$$S = \frac{\Delta f}{\Delta x}, \quad (19)$$

$$\text{FOM} = \frac{S}{\text{FWHM}}, \quad (20)$$

$$\text{DL} = \frac{f_T}{20SQ}, \quad (21)$$

where Δf and Δx refer to the differences in frequency and the sensing quantity. f_T implies the f value of the AP.

When the phase difference $\Delta\varphi_2$ is fixed at 0°, as can be seen from Fig. 8, the frequency point of the AP varies in a strong linear relationship with the value of n_D in the range of 1.34–1.355. In the detection range, the APs are always larger than 0.9, which can ensure the quality of the OBM. The LFR is produced by utilizing the linear fitting method at equidistant points along the horizontal axis. In addition, the statistical measure R-square,[28] which is used to evaluate the goodness of fit in a mathematical regression model, is added to this paper for a clearer analysis of LFR performance. It serves as a crucial indicator of the dependability belonging to the OBM. The closer the R-square is to 1, the better capability the OBM has.[28]
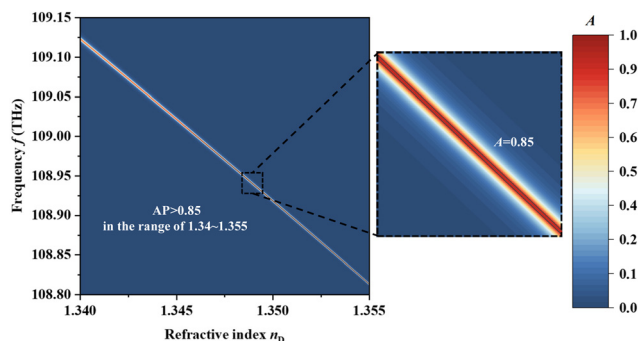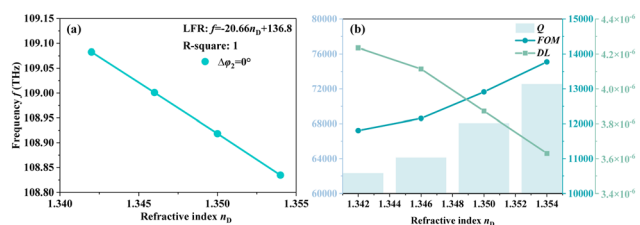
Fig. 9 shows the indices of the OBM for the RI detection in the range of 1.34–1.55 when $\Delta\varphi_2$ is controlled to 0°. In the measured range, the LFR is $f = -20.66n_D + 136.8$, which is

Table 3 The RI of detection cell types when $\Delta\varphi_2$ is controlled to 0°[29]

Type	RI (RIU)	Error (RIU)
RK3E	1.347	6.0×10^{-3}
RK3E-ras	1.373	1.6×10^{-2}
INOK	1.343	7.0×10^{-3}
YD-10B	1.369	1.0×10^{-2}

Fig. 8 The top view of the AP varies with the value of n_D in the case of $\Delta\varphi_2$ fixed at 0°.

Fig. 9 The indices of the OBM for the RI detection when $\Delta\varphi_2$ is fixed at 0°. (a) LFR between n_D and f. (b) The Q, FOM, and DL under different values of n_D in the range of 1.34–1.355.

shown in Fig. 9(a), and the value of S is 20.66 THz RIU^{-1}. The R-square up to 1 proves that the excellent linearity is satisfied between n_D and f. As can be seen from Fig. 9(b), in the detection range, the values of Q, FOM, and DL are, respectively, about 6.9×10^4, 1.2×10^3 RIU^{-1}, and 3.6×10^{-6} RIU. According to the sensing range and the performance indices in the case of $\Delta\varphi_2$ fixed at 0°, the proposed OBM in this mode has the ability to distinguish rat kidney cells and human oral squamous cells[29] (see Table 3) accurately. Because the RIs of normal cells are in the detection range of 1.34–1.55, and the RIs of these cancer cells are out of the detection range. The presence of sharp APs indicates that the detection sample is normal cells when the f is in the working range of 108.8–109.1 THz. If in the working range sharp APs are absent, it means the cells may mutate into cancer cells.

Fig. 10 shows that the f value of the AP fluctuates in a strong linear relationship with the value of n_D in the range of 1.659–1.662. Because the value of A of the AP which is within the measured range is always larger than 0.9. The quality of the

4452 | *Phys. Chem. Chem. Phys.*, 2024, **26**, 4447–4454

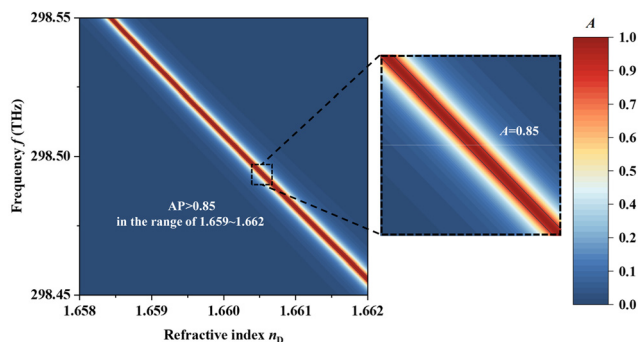This journal is © the Owner Societies 2024

Fig. 10 The top view of the AP varies with the value of n_D in the case of $\Delta\varphi_2$ fixed at 180°.

OBM is good. In addition to utilizing the method of linear fitting, the LFR between n_D and f is established in Fig. 11(a) with the $\Delta\varphi_2$ set to 180°. Within the detection range, the excellent linearity is satisfied between the n_D and f, with R-square up to 1, and the LFR is $f = -26.57n_D + 342.6$, indicating that S is 26.57 THz RIU^{-1}. Fig. 11(b) provides a graphical representation of the key parameters obtained from the analysis. The values of Q, FOM, and DL are approximately 7×10^4, 6×10^3 RIU^{-1}, and 1×10^{-5} RIU, respectively. These results further highlight that the OBM with CPA is valuable in biosensing applications.

Based on the detection range and the data of high-performance indices in the case of $\Delta\varphi_2$ fixed at 180°, the OBM in this mode has the function of distinguishing human gastric cells, human liver cells, and human epidermal cells[30] (see Table 4) clearly. Because the RIs of the measured cells are in the detection range of 1.659–1.662. In the working frequency range of 298.45–298.55 THz, the OBM can detect the type of these cells through the movement of f with the help of the LFR $f = -26.57n_D + 342.6$.

According to the research discussion above, the proposed OBM with a high Q, great FOM, and low DL has good performance in distinguishing cancer cells. Moreover, the OBM can change the RI detection ranges including the RIs of different cancer cells by controlling the phase difference. Therefore, the given OBM can realize the function of sensing multiple cancer cells. Due to the ability of efficient and precise detection of the RI, it can be widely used in the biomedical field like in the concentration detection of glucose aqueous solution and detection of single waterborne bacteria.[31,32]
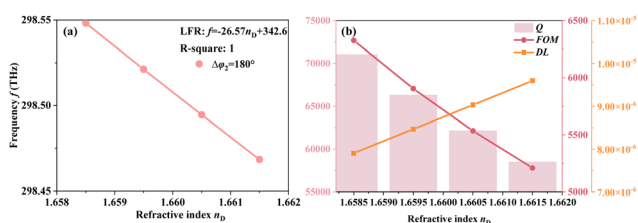
Table 5 Comparison of previous works with the proposed OBM in terms of performance

Ref.	Q	Variable sensing range	CPA	Phase control	Approach
Ref. 30	12750	No	No	No	ROTE
Ref. 33	100	No	No	No	2-D PC
Ref. 34	92	No	No	No	3-D OBM
Ref. 35	11.33	No	No	No	High field confinement
This work	69 000 and 70 000	Yes	Yes	Yes	CPA

To logically and methodically show the innovations of the OBM, Table 5 lists some related works (cancer cell detection based on optical RI sensing) done before and compares this work with them. The obtained high Q enables more accurate detection of cancer cells. Furthermore, as can be seen from Table 5, based on the principle of CPA, the OBM has the ability to control phase and multiple detection ranges.

4. Conclusion

In summary, an OBM based on CPA, given in this paper, can realize the ability to detect multiple cancer cells effectively and accurately. By establishing a particular linear relationship between n_D and f, it transforms the biological signal of a cancer cell into a photoelectric signal. The detection of slight changes in the RI of cancer cells is possible, thanks to the high Q, great FOM, and low DL of the OBM, whose best values are, respectively, 6.9×10^4, 1.2×10^3 RIU^{-1}, and 3.6×10^{-6} RIU. In addition, its S can reach 26.57 THz RIU^{-1}. Additionally, based on the principle of CPA, the OBM can realize the function of multiple cancer cell detection by adjusting the sensing range by controlling the phase difference of coherent EWs. Compared with some related works done before, this work has major implications for advancing the study and investigation into the application of CPA. It provides a new approach to distinguishing cancer cells. It also may be widely used in the biomedical field like in the identification of single aquatic bacteria and the quantity of glucose in an aqueous solution.

Conflicts of interest

There are no conflicts to declare.

Acknowledgements

Fig. 11 The indices of the OBM for the RI detection when $\Delta\varphi_2$ is fixed at 180°. (a) LFR between n_D and f. (b) Q, FOM, and DL under different values of n_D in the range of 1.658–1.662.

Notes and references

1 W. Wan, Y. Chong, L. Ge, H. Noh, A. D. Stone and H. Cao, *Science*, 2011, **331**, 889–892.

This journal is © the Owner Societies 2024

Phys. Chem. Chem. Phys., 2024, **26**, 4447–4454 | **4453**

2 Y. D. Chong, Coherent Perfect Absorbers: Time-Reversed Lasers, *Phys. Rev. Lett.*, 2010, **105**, 053901.

3 S. Zanotto, F. Bianco, V. Miseikis, D. Convertino, C. Coletti and A. Tredicucci, Coherent absorption of light by graphene and other optically conducting surfaces in realistic on-substrate configurations, *APL Photonics*, 2016, **2**, 016101.

4 A. Xomalis, I. Demirtzioglou, E. Plum, Y. Jung, V. Nalla, C. Lacava, K. F. MacDonald, P. Petropoulos, D. J. Richardson and N. I. Zheludev, Fibre-optic metadevice for all-optical signal modulation based on coherent absorption, *Nat. Commun.*, 2018, **9**, 182.

5 J. H. Zou, J. Y. Sui, Q. Chen and H. F. Zhang, Arithmetic logic unit based on the metastructure with coherent absorption, *Opt. Lett.*, 2023, **48**, 5699–5702.

6 S. Dey, S. Singh and D. N. Rao, High precision position sensor based on CPA in a composite multi-layered system, *Opt. Express*, 2018, **26**, 10079–10090.

7 Y.-R. Wu, R.-Y. Dong, J. Xu and H.-F. Zhang, A novel CPA-based layered photonic structure for multipurpose sensing applications, *Opt. Laser Technol.*, 2023, **163**, 109422.

8 J. Zugazagoitia, C. Guedes, S. Ponce, I. Ferrer, S. Molina-Pinelo and L. Paz-Ares, Current Challenges in Cancer Treatment, *Clin. Ther.*, 2016, **38**, 1551–1566.

9 K. Pantel, C. Alix-Panabières and S. Riethdorf, Cancer micrometastases, *Nat. Rev. Clin. Oncol.*, 2009, **6**, 339–351.

10 M. B. Sporn, The war on cancer, *Lancet*, 1996, **347**, 1377–1381.

11 R. Mohammadi, H. Naderi-Manesh, L. Farzin, Z. Vaezi, N. Ayarri, L. Samandari and M. Shamsipur, Fluorescence sensing and imaging with carbon-based quantum dots for early diagnosis of cancer: A review, *J. Pharm. Biomed. Anal.*, 2022, **212**, 114628.

12 R. Barer, K. F. A. Ross and S. Tkaczyk, Refractometry of living cells, *Nature*, 1953, **171**, 720–724.

13 A. Ahmadivand and B. Gerislioglu, Photonic and plasmonic metasensors, *Laser Photonics Rev.*, 2022, **16**, 2100328.

14 S. Romano, A. Lamberti, M. Masullo, E. Penzo, S. Cabrini, I. Rendina and V. Mocella, Optical Biosensors Based on Photonic Crystals Supporting Bound States in the Continuum, *Materials*, 2018, **11**, 526.

15 S. Ghorbani, M. Sadeghi and Z. Adelpour, A highly sensitive and compact plasmonic ring nano-biosensor for monitoring glucose concentration, *Laser Phys.*, 2019, **30**, 026204.

16 J. Sui, R. Dong, S. Liao, Z. Zhao, Y. Wang and H.-F. Zhang, Janus Metastructure Based on Magnetized Plasma Material with and Logic Gate and Multiple Physical Quantity Detection, *Ann. Phys.*, 2023, **535**, 2200509.

17 F. Zhang, S. Feng, K. Qiu, Z. Liu, Y. Fan, W. Zhang, Q. Zhao and J. Zhou, Mechanically stretchable and tunable meta-material absorber, *Appl. Phys. Lett.*, 2015, **106**, 091907.

18 J. R. DeVore, Refractive Indices of Rutile and Sphalerite, *J. Opt. Soc. Am.*, 1951, **41**, 416–419.

19 H. H. Li, Refractive index of alkaline earth halides and its wavelength and temperature derivatives, *J. Phys. Chem. Ref. Data*, 1980, **9**, 161–290.

20 I. H. Malitson, Interspecimen Comparison of the Refractive Index of Fused Silica, *J. Opt. Soc. Am.*, 1965, **55**, 1205–1209.

21 A. K. Geim, Graphene: Status and Prospects, *Science*, 2009, **324**, 1530–1534.

22 E. Carrasco, M. Tamagnone, J. R. Mosig, T. Low and J. Perruisseau-Carrier, Gate-controlled mid-infrared light bending with aperiodic graphene nanoribbons array, *Nanotechnology*, 2015, **26**, 134002.

23 S. Guo, C. Hu and H. Zhang, Ultra-wide unidirectional infrared absorber based on 1D gyromagnetic photonic crystals concatenated with general Fibonacci quasi-periodic structure in transverse magnetization, *J. Opt.*, 2020, **22**, 105101.

24 A. Andryieuski and A. V. Lavrinenko, Graphene metamater-ials based tunable terahertz absorber: effective surface conductivity approach, *Opt. Express*, 2013, **21**, 9144–9155.

25 X.-Y. Liang, N. Ding, S.-P. Ng and C.-M. L. Wu, Adsorption of gas molecules on Ga-doped graphene and effect of applied electric field: A DFT study, *Appl. Surf. Sci.*, 2017, **411**, 11–17.

26 L. Qi, Z. Yang, F. Lan, X. Gao and Z. Shi, Properties of obliquely incident electromagnetic wave in one-dimensional magnetized plasma photonic crystals, *Phys. Plasmas*, 2010, **17**, 042501.

27 W. Zhu, F. Xiao, M. Kang and M. Premaratne, Coherent perfect absorption in an all-dielectric metasurface, *Appl. Phys. Lett.*, 2016, **108**, 121901.

28 B.-F. Wan, Q.-Y. Wang, H.-M. Peng, H.-N. Ye and H.-F. Zhang, A Late-Model Optical Biochemical Sensor Based on OTS for Methane Gas and Glucose Solution Concentration Detection, *IEEE Sens. J.*, 2021, **21**, 21465–21472.

29 W. J. Choi, D. I. Jeon, S.-G. Ahn, J.-H. Yoon, S. Kim and B. H. Lee, Full-field optical coherence microscopy for identifying live cancer cells by quantitative measurement of refractive index distribution, *Opt. Express*, 2010, **18**, 23285–23295.

30 A. Jian, M. Jiao, Y. Zhang, Q. Zhang, X. Xue, S. Sang and X. Zhang, Enhancement of the volume refractive index sensing by ROTE and its application on cancer and normal cells discrimination, *Sens. Actuators, A*, 2020, **313**, 112177.

31 S. Ghorbani, M. Sadeghi and Z. Adelpour, A highly sensitive and compact plasmonic ring nano-biosensor for monitoring glucose concentration, *Laser Phys.*, 2019, **30**, 026204.

32 P. Y. Liu, L. K. Chin, W. Ser, T. C. Ayi, P. H. Yap, T. Bourouina and Y. Leprince-Wang, An optofluidic imaging system to measure the biophysical signature of single water-borne bacteria, *Lab Chip*, 2014, **14**, 4237–4243.

33 A. Panda and P. P. Devi, Photonic crystal biosensor for refractive index based cancerous cell detection, *Opt. Fiber Technol.*, 2020, **54**, 102123.

34 S. Banerjee, P. Dutta, A. V. Jha, B. Appasani and M. S. Khan, A Biomedical Sensor for Detection of Cancer Cells Based on Terahertz Metamaterial Absorber, *IEEE Sens. Lett.*, 2022, **6**, 1–4.

35 M. Y. Azab, M. F. O. Hameed, A. M. Nasr and S. S. A. Obayya, Highly sensitive metamaterial biosensor for cancer early detection, *IEEE Sens. J.*, 2021, **21**, 7748–7755.

4454 | *Phys. Chem. Chem. Phys.*, 2024, **26**, 4447–4454

This journal is © the Owner Societies 2024